Controlled Growth of Platinum Nanoparticles on Strontium Titanate Nanocubes by Atomic Layer Deposition

*Steven T. Christensen, Jeffrey W. Elam, Federico A. Rabuffetti, Qing Ma, Steven J. Weigand, Byeongdu Lee, Soenke Seifert, Peter C. Stair, Kenneth R. Poeppelmeier, Mark C. Hersam, and Michael J. Bedzyk**

***W**ith an eye toward using surface morphology to enhance heterogeneous catalysis, Pt nanoparticles are grown by atomic layer deposition (ALD) on the surfaces of $SrTiO_3$ nanocubes. The size, dispersion, and chemical state of the Pt nanoparticles are controlled by the number of ALD growth cycles. The $SrTiO_3$ nanocubes average 60 nm on a side with {001} faces. The Pt loading increases linearly with Pt ALD cycles to a value of 1.1×10^{-6} g cm^{-2} after five cycles. Scanning electron microscopy images reveal discrete, well-dispersed Pt nanoparticles. Small- and wide-angle X-ray scattering show that the Pt nanoparticle spacing and size increase as the number of ALD cycles increases. X-ray absorption spectroscopy shows a progression from platinum(II) oxide to metallic platinum and a decrease in Pt–O bonding with an increase in Pt–Pt bonding as the number of ALD cycles increases.*

Keywords:
- atomic layer deposition
- nanoparticles
- platinum
- strontium titanate
- X-ray analysis

1. Introduction

Nanometer-sized noble-metal particles supported on metal oxide surfaces can serve as effective heterogeneous catalysts for accelerating electrochemical,[1–3] photochemical,[4,5] and thermal processes.[6,7] Effective nanosized noble-metal catalysts may help to achieve goals in both energy production and conservation as well as in reducing pollution.[8,9] There exists a need for scalable synthetic methods to prepare well-dispersed nanoparticles on complex support geometries, such as aerogels, porous structures, and other nanoparticles. Efficient loading of the noble-metal catalyst remains a critical issue in the economic viability of these catalyst architectures. Atomic layer deposition (ALD) is a promising technique for catalyst manufacturing.[10,11]

In the ALD process, a substrate is alternately exposed to different reactive precursor vapors, which react in a self-limiting manner to deposit materials in an atomic layer-by-layer fashion. Although this process typically results in uniform, continuous layers, the ALD of noble metals, such as Pt, has been shown to generate nanoparticles during the initial stages of growth.[12–15] Consequently, ALD can be used to deposit well-dispersed noble-metal nanoparticles for catalysis.[2,13,14] The self-limiting surface chemical reactions and diffusion of the precursor gases render this method easily scalable.[11]

[*] Prof. M. J. Bedzyk, Dr. S. T. Christensen, Prof. M. C. Hersam
Department of Materials Science and Engineering
Northwestern University
Evanston, IL 60208-3108 (USA)
E-mail: bedzyk@northwestern.edu
Dr. J. W. Elam
Energy Systems Division
Argonne National Laboratory
Argonne, IL 60439 (USA)
F. A. Rabuffetti, Prof. P. C. Stair, Prof. K. R. Poeppelmeier, Prof. M. C. Hersam
Department of Chemistry
Northwestern University
Evanston, IL 60208-3108 (USA)
Dr. Q. Ma, Dr. S. J. Weigand
DND CAT – Synchrotron Research Center
Northwestern University
Evanston, IL 60208 (USA)
Dr. B. Lee, Dr. S. Seifert
X-ray Science Division
Argonne National Laboratory
Argonne, IL 60439 (USA)

DOI: 10.1002/smll.200801920

small NANO MICRO

It has been recognized that ALD offers the potential for rational catalyst design from first-principles calculations,[16] but such an undertaking requires a detailed knowledge of how noble-metal nanoparticles nucleate and grow on metal oxide surfaces. In particular, the growth process should be understood at the length scale of nanometers or smaller. To this end, herein we report an investigation of the nucleation and growth of the deposited Pt nanoparticles (termed ALD Pt) by utilizing nanoscale diagnostic probes. In this study, we use cube-shaped strontium titanate ($SrTiO_3$; STO) nanoparticle substrates prepared by sol precipitation–hydrothermal treatment because these serve as a realistic, high-surface-area support that is appropriate for catalytic testing.[17]

The Pt/STO system has been studied as a model photocatalyst for fuel production.[18–20] Recently, ALD Pt/STO nanocubes have shown favorable results as a combustion catalyst.[21] The success of the Pt/STO system in these applications lies in the $SrTiO_3$ support. Due to comparable bandgaps, $SrTiO_3$ acts as a UV photocatalyst similar to TiO_2,[22] in which photons generate electron–hole pairs that catalyze reactions to produce fuels such as hydrogen or methanol. In oxidative catalysis, STO as a support material can reduce unwanted carbonaceous buildup.[23] The nucleation of ALD Pt on the STO nanocubes[17,24] is of particular interest as ALD offers some advantages in cleanliness and precision when compared to traditional catalyst preparation methods. Since STO nanocube faces are reported to have the {001} orientation, the Pt/STO nanocube system may be readily compared to our previous study of Pt ALD on planar, single-crystal $SrTiO_3$ (001).[25]

The original studies of the ALD of Pt using alternating exposures to (methylcyclopentadienyl)trimethylplatinum(IV) ($MeCpPtMe_3$) and oxygen concluded that this method results in metallic Pt films; however, these investigations did not look in detail at the early stages of growth.[26,27] In particular, the chemical state, size, and dispersion of the platinum nanoparticles were not explicitly addressed but rather the studies focused on the steady-state growth after several hundred ALD cycles. The nature of the Pt in the early stages of growth remains an open question, and the nature of the underlying support surface is bound to play a critical role in affecting the Pt. For instance, in our recent report, we described how the ALD Pt growth rate is higher than expected on $SrTiO_3$ (001) and asserted that the STO surface catalyzes the reaction of the $MeCpPtMe_3$ precursor, and furthermore that Pt surface diffusion plays an important role in the nucleation process.[25]

These findings raise key issues for synthesizing Pt nanoparticles on $SrTiO_3$ and other substrate materials by using ALD. One of the key issues in the early stages of platinum ALD is the final Pt oxidation state. The conversion of platinum from the +4 oxidation state in the $MeCpPtMe_3$ precursor to the zero-valent bulk metallic chemical state on $SrTiO_3$ nanocubes offers an intriguing opportunity to study and adapt ALD-grown nanostructures for applications in catalysis and fuel-cell technologies.

Herein, we utilize the high-resolution imaging capabilities of scanning electron microscopy (SEM) to confirm the nanoparticle morphology and dispersion. The platinum nanoparticle dispersion and size are further explored with small-angle X-ray scattering (SAXS) and wide-angle X-ray scattering (WAXS), respectively. The chemical state and the local atomic coordination of the platinum nanoparticles are studied by X-ray absorption spectroscopy (XAS), the former of which is revealed by the X-ray absorption near-edge structure (XANES) and the latter by the extended X-ray absorption fine structure (EXAFS).

2. Results

2.1. Mass Gain

The uncoated $SrTiO_3$ nanoparticles are nonporous, single-crystalline, cube-shaped particles having the {001} faces primarily exposed, with an average edge length of 60 nm, and a Brunauer–Emmett–Teller surface area of 20 $m^2\ g^{-1}$.[17] Measuring the mass gain for the cases of one to five Pt ALD growth cycles yielded a linear increase of 4.4 wt% Pt per cycle. By using the $SrTiO_3$ surface area of 20 $m^2\ g^{-1}$ and the previously observed Pt ALD growth rate of 0.5 Å per cycle,[27] the expected mass gain is 2.1 wt% per cycle. The measured weight gain is larger by twofold, which indicates a higher initial growth rate for ALD Pt on the $SrTiO_3$ surface as compared to the Pt surface. Growth rates in ALD are typically dictated by the number of ligands, which remain on the surface following adsorption of the metal precursor because these ligands will prevent the adsorption of additional precursor molecules. This growth rate is not altogether unexpected, as our recent work on ALD Pt films on single-crystal $SrTiO_3$ (001) showed a similar increased growth rate prior to film closure.[25] The $SrTiO_3$ appears to catalyze the ALD leading to an increased growth rate until a complete film forms.

2.2. Scanning Electron Microscopy

Figure 1 shows SEM images of the $SrTiO_3$ nanocubes recorded before and after three Pt ALD cycles. Comparison of these images clearly reveals the presence of Pt nanoparticles resulting from the ALD treatment. The Pt particles appear to be 2–3 nm in size, which is at the resolution limit of the microscope. The Pt nanoparticles are uniformly dispersed on all exposed surfaces of the $SrTiO_3$ nanocubes with a 4–8 nm interparticle spacing.

2.3. X-ray Scattering

The SAXS data are plotted in Figure 2 for the five Pt ALD cases and the blank $SrTiO_3$ nanocubes without Pt. The data

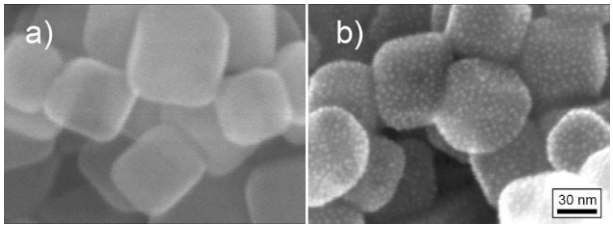

Figure 1. SEM images of STO nanocubes before (a) and after (b) coating with Pt nanoparticles using three Pt ALD growth cycles.

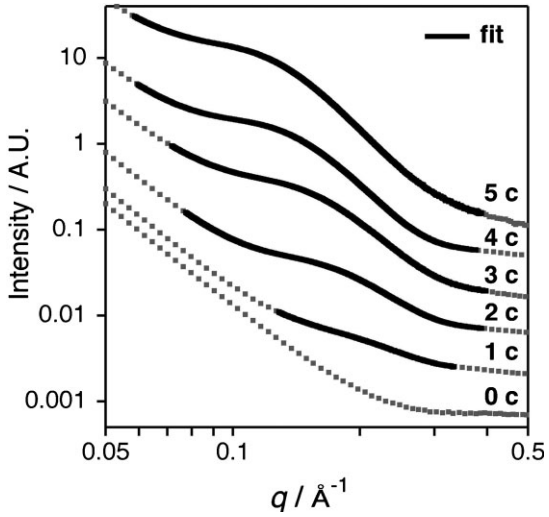

Figure 2. SAXS data showing the interparticle scattering interference for the Pt nanoparticles (offset for clarity). The interference leads to a peak, the position of which yields the interparticle spacing by using Equation (1). The data show a dependence on the number of ALD cycles (0–5 c) for the position of the peak, which has been fitted with a pseudo-Voigt function on a power-law background (solid lines).

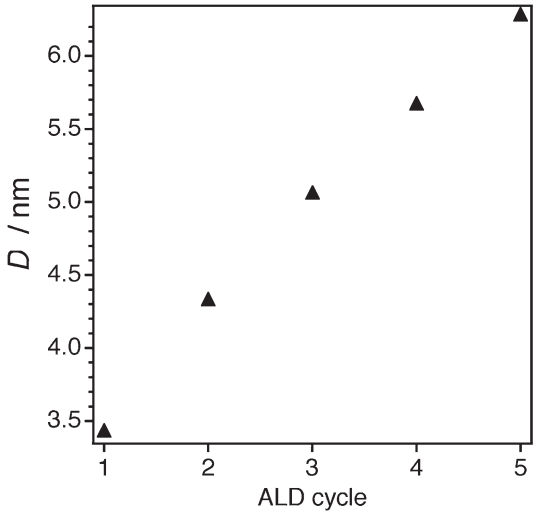

Figure 3. Center-to-center interparticle spacing (D) determined from the fits shown in Figure 2 and using Equation (1). The linear dependence of D on the ALD cycle shows that the number density of nanoparticles is decreasing due to nanoparticle coalescence.

show a broad peak at a scattering vector magnitude of $q \approx 0.15$ Å^{-1}, which is due to the constructive interference from waves scattered by neighboring platinum nanoparticles and is related to the average center-to-center spacing (D) between the nanoparticle as

$$D = \frac{2\pi}{q_p} \quad (1)$$

The peak position q_p shows a distinct dependence on the number of ALD cycles. Fitting a pseudo-Voigt function with a power-law background enables the determination of the peak position; the solid lines in Figure 2 represent the peak fits. The fitting results are plotted against the ALD cycle in Figure 3. The interparticle spacing increases in a linear fashion from 3.5 to 6.3 nm as the number of ALD cycles increases and follows a linear growth law. A linear increase of the center-to-center particle spacing indicates that the number density of particles per unit area is decreasing, which is due to the particles coalescing.

The WAXS is equivalent to the powder diffraction from the nanocubes and platinum nanoparticles. An example of the diffraction pattern is shown in Figure 4 for the uncoated $SrTiO_3$ nanocubes, where the Bragg peaks have been indexed. The room-temperature lattice constants of 3.924 Å for cubic-F Pt and 3.905 Å for cubic-P $SrTiO_3$ are such that the broadened Pt Bragg peaks overlap those of $SrTiO_3$. By using the Scherrer equation[28] the mean crystallite size (t_H) in the $H = hkl$ direction can be determined from the full width at half maximum (FWHM or Δq) of the peak as

$$t_H = 0.9^* \frac{2\pi}{\Delta q} \quad (2)$$

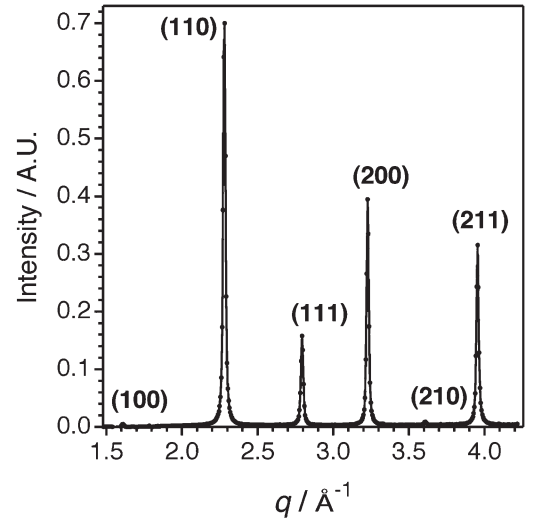

Figure 4. WAXS data for uncoated $SrTiO_3$ nanocubes. The Bragg peaks have been indexed. The positions and relative intensities of the peaks are consistent with polycrystalline cubic-P $SrTiO_3$ with $a = 3.90$ Å.

The uncoated $SrTiO_3$ nanocubes were inspected for line broadening and showed a ≈40 nm domain size from the (110), (111), (200), and (211) peaks. This compares to the ≈60 nm nanoparticle size from microscopy in Figure 1 and indicates that the $SrTiO_3$ nanocubes are single crystals. Figure 5 shows the (111) Bragg peak for the five ALD cycle and blank $SrTiO_3$ cases, in which broadening due to the platinum nanoparticles can be observed. The peak shape was fitted using a double Lorentzian function given by

$$f(q) = A^* \left[\frac{(1-\phi)}{1 + \frac{q-q_1}{b_1^2}} + \frac{\phi}{1 + \frac{q-q_0}{b_0^2}} \right] \quad (3)$$

where A is a scaling parameter, ϕ is a mixing parameter between the two Lorentzians, and the q and b terms give the

small NANO MICRO

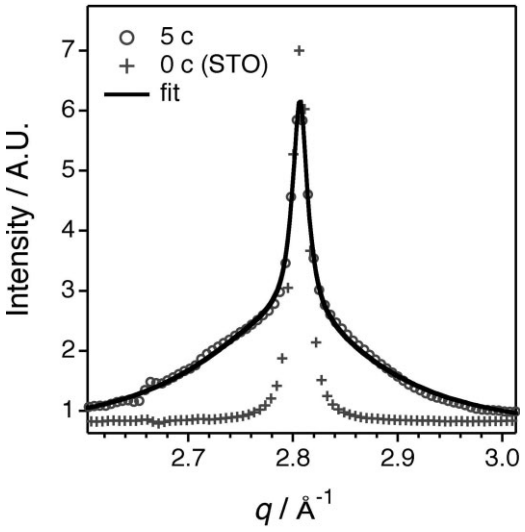

Figure 5. Line broadening effects of the (111) diffraction peak due to the Pt nanoparticle size for the case of five Pt ALD cycles. An uncoated $SrTiO_3$ pattern (0 c) has been overlaid to illustrate the effect. The broadening was fitted to Equation (3) where the FWHM measured for the Pt nanoparticles could yield the crystallite size by using Equation (2).

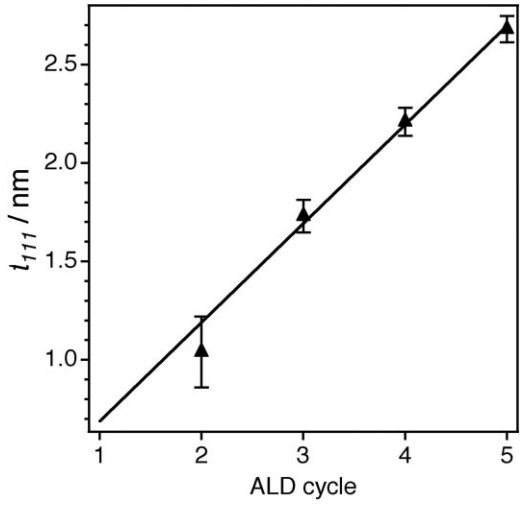

Figure 6. Platinum domain crystallite size (t_{111}) determined from line-shape analysis of the WAXS data, like that displayed in Figure 5. The linear growth trend is consistent with nanoparticle growth for ALD.

peak positions and widths, respectively. The domain size is then determined by using Equation (2) and the 2^*b_0 term for the FWHM of a Lorentzian. The broadening for the Pt(200) peaks was not as marked and consequently did not yield useful information. Figure 6 plots the Pt crystallite size for the (111) peak for two to five ALD cycles, which shows that t_{111} increases from 1.0 to 2.7 nm and again shows a linear growth trend. The line width for the one-cycle case was too large to determine the particle size, but based on the linear regression for the other cases, the particle size would be ≈0.7 nm.

2.4. X-ray Absorption Spectroscopy

XANES in the set of X-ray absorption spectra shown in Figure 7 indicates a change in the chemical state of the

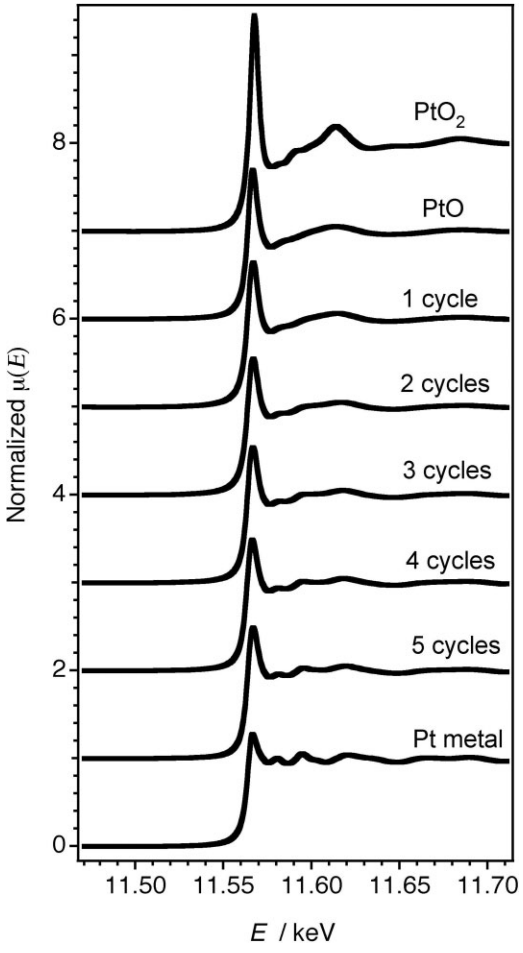

Figure 7. Normalized X-ray absorption cross sections for the five ALD samples, a Pt foil reference, a platinum(II) oxide reference, and a platinum(IV) oxide reference. The line shape of the spectra suggests that at one ALD cycle the platinum is in a similar state to platinum in PtO and as the number of ALD cycles increases, the platinum chemical state progresses to that of Pt metal. Fitting of the ALD spectra to a linear combination of the Pt foil reference and PtO reference produced the results in Table 2.

platinum as the number of Pt ALD growth cycles changes. The normalized absorption cross sections of Figure 7 include the five ALD cases, a platinum-metal foil, and two platinum oxides: PtO and PtO_2. The measured Pt L_3 absorption edges (relative to $E_0 = 11\,564$ eV) are given in Table 1. The three-, four-, and five-cycle cases show no significant shift in E_0, whereas the one- and two-cycle cases show a shift of $\Delta E_0 = +1$ eV, which is consistent with oxidized platinum. In addition to the edge position, the XANES region ($E_0 - 100\,\text{eV} < E < E_0 + 40\,\text{eV}$) provides additional information regarding the chemical state of the Pt. The line shape of the one-cycle platinum XANES sample compares favorably with that of the PtO standard shown in Figure 7. The XANES then transitions to that of bulk metallic platinum as the number of cycles increases. In addition to the ΔE_0 shift from E_0 mentioned above, the white-line intensity increases as the number of ALD cycles decreases. The white-line intensity in this case is related to the d-electron density of states. An

Table 1. XAS analysis results for the five ALD samples and references. The Pt L_3 absorption edge ($E_0 = 11\,564$ eV) shifts to higher energy as the platinum becomes oxidized. Also given are the EXAFS fitting results, which show an increase in the Pt coordination (N_{Pt}) and Pt–Pt bond length (r_{Pt-Pt}) as the number of ALD cycles increases.

Sample	Pt L_3 edge shift	EXAFS fitting	
	ΔE_0 [eV]	N_{Pt}	r_{Pt-Pt} [Å]
PtO_2	+2	n.a.[a]	n.a.
PtO	+1	n.a.	n.a.
1 cycle	+1	0.2	2.70 ± 0.05
2 cycles	+1	1	2.72 ± 0.02
3 cycles	0	2.6	2.74 ± 0.01
4 cycles	0	3.7	2.74 ± 0.01
5 cycles	0	4.4	2.75 ± 0.01
Pt foil	0	12	2.76 ± 0.01

[a] n.a. = not applicable.

increase in the white-line intensity indicates a decrease in the number of electrons in the d orbital. A reduction of the d-electron density of states would be consistent with the oxidation of platinum. A linear combination fit of the XANES of the samples using the Pt and PtO XANES spectra leads to the results given in Table 2. As the number of ALD cycles increases, the Pt–Pt bond increases from 10 to 57% at the expense of the Pt–O bond.

The Fourier transforms of the EXAFS region ($E_0 + 40\ \text{eV} < E < E_0 + 1000\,\text{eV}$) are plotted in Figure 8 for the various cases. Here, the Pt–O bond is evident at one cycle and steadily diminishes as the Pt–Pt bond becomes more prevalent. The Pt–Pt bond was fitted using the ARTEMIS program[29] in *R*-space over a wave vector (k) range of 8–13.95 $Å^{-1}$ and a k-weight factor of k^2. The fitting results given in Table 1 show the effect of the platinum coverage, where the coordination (N_{Pt}) and the Pt–Pt bond length (r_{Pt-Pt}) increase with each ALD cycle. The Pt coordination also increases effectively from zero to 4.4 as the ALD cycles increase.

For the Pt–O bond, the best results were obtained with a slightly different fitting approach. Using the XANES linear combination results from Table 2, the fraction of the Pt foil spectrum was subtracted from the ALD spectra to yield a partial absorption cross section. This cross section was then fitted using ARTEMIS to extract the Pt–O bond length for the various cases. The fitting for Pt–O occurred over a k range of 3–7.8 $Å^{-1}$, where the oxygen backscattering amplitude

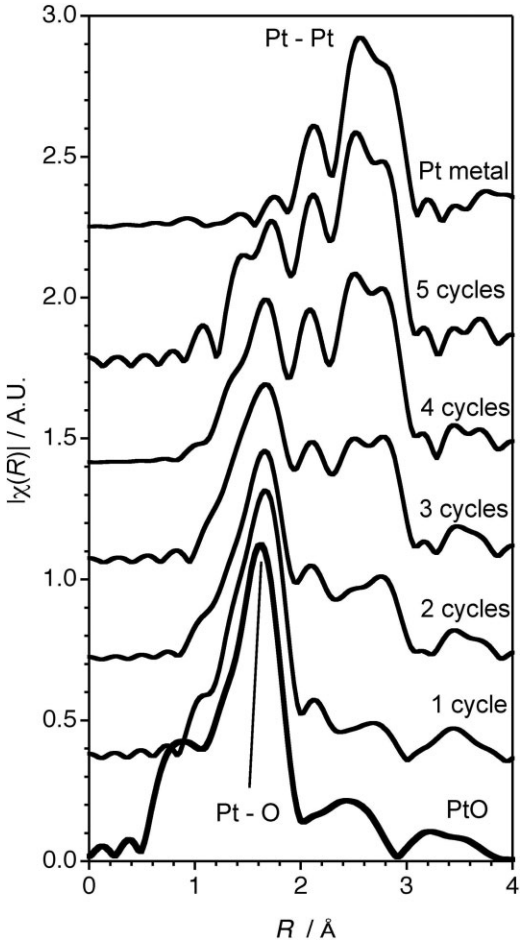

Figure 8. Magnitude of the Fourier transform of the EXAFS for Pt–Pt and Pt–O bonding. As the number of ALD cycles increases, the Pt–O bond diminishes as the Pt–Pt bond increases. These data were fitted to produce the results reported in Table 1.

essentially locates, and a k-weight factor of k^1. For all cases, the Pt–O bond length was determined to be $r_{Pt-O} = 1.98 \pm 0.03$ Å. The Pt–O bond length for a tetragonal PtO crystal structure[30] is 2.04 Å with a coordination (N_{PtO}) of 4. The Pt–O coordination from the data could not be obtained reliably due to the method of using partial absorption cross sections.

Table 2. XANES spectra of the ALD samples shown in Figure 7 are fitted to a linear combination of the Pt foil and PtO reference spectra to determine the relative amount of Pt in the bulk metallic and oxidized chemical states.

Sample	% Pt	% PtO
1 cycle	10	90
2 cycles	23	77
3 cycles	35	65
4 cycles	48	52
5 cycles	57	43

3. Discussion

The discrete nanoparticles observed in the SEM images of Figure 1 are consistent with the results for ALD Pt on aerogels reported by King et al., where the Pt loading was on the order of 0.05 mg cm^{-2}.[14] This Pt loading is less than the 1 mg cm^{-2} projected by Liu et al. as the target for the economic viability of direct methanol fuel cells.[1] We can compare these figures to our results in two ways. First, using the 20 $m^2\ g^{-1}$ surface of the STO nanocubes and the 4.4 wt% Pt per ALD growth cycle from the mass gain, the Pt loading is 1.1×10^{-3} mg cm^{-2} for five ALD cycles. The Pt loading (Θ) may also be calculated from the SAXS and WAXS analysis by using the following

relationship [Eq. (4)]:

$$\Theta = \frac{V_p \rho}{D^2} \quad (4)$$

where V_p is the particle volume and ρ is the mass density. For the case of five ALD cycles in which the mean nanoparticle size $t_{111} = 3$ nm and mean center-to-center distance $D = 6$ nm, a hemispherical particle at the bulk density of platinum (21.45 g cm^{-3}) would give $\Theta \approx 3 \times 10^{-3}$ mg cm^{-2}, which is in reasonable agreement with the measured weight gain.

Nanoparticles of this size range are likely to show a size–property relationship for which chemical activity will vary appreciably over a few nanometers.[31–33] Related to size–property effects are changes in the catalyst bonding and chemical state. The X-ray scattering data show that the Pt nanoparticle size and spacing correlate with the number of ALD growth cycles. Consequently, we can relate the coordination, bond properties, and chemical state to the size of the nanoparticle. The data show a contraction of the Pt–Pt bond as the nanoparticle size (ALD cycles) decreases. Bond contractions of this nature have been observed for platinum[34,35] and could play an important role in the catalytic activity, as has been demonstrated with gold nanoparticles.[36]

The chemical state of the nanoparticle becomes an interesting area to investigate when considering the effects of size on nanoparticle properties. However, changes in platinum activity could be expected through a different mechanism, as the gold nanoparticle study by Miller et al. concluded an electron enrichment of the d orbitals. For the ALD Pt, the white-line intensity increases indicating that the d orbitals are losing electrons. The position of E_0 for ALD Pt also suggests that the Pt is oxidized for at least one and two ALD cycles. The oxidation is also evident in the reduced Pt coordination for the cases with fewer ALD cycles from the EXAFS fitting. Mukerjee and McBreen used XAS measurements to conclude that the reduced Pt coordination for smaller nanoparticles facilitated the adsorption of OH and CO, which correlated with reduced catalyst activity.[32] With this in mind, we can now explore the oxidation of the ALD Pt nanoparticles in regard to the conversion of the ALD precursor, the role of the $SrTiO_3$ substrate, and interaction with the environment upon removal from the ALD reactor.

For metallic ALD materials, the chemical state also becomes important to confirm conversion from the organometallic precursor to metallic film. In previous studies of Pt ALD using O_2 and $MeCpPtMe_3$, the conversion was high and the metallic Pt state was observed.[15,25–27,37] These conclusions are based on measuring the reaction products, and on spectroscopy and electrical resistivity measurements. The oxidation of the platinum nanoparticles may be due less to the conversion of $MeCpPtMe_3$ and more to the role of the STO substrate and the environment.

To investigate the effect of the STO nanocubes, we considered density functional theory (DFT) calculations for the Pt/$SrTiO_3$ (001) system.[38] The DFT modeling indicates that the Pt will prefer to bind to the lattice oxygen and that the stability of the Pt/$SrTiO_3$ structure improved as the Pt–O bond length approached ≈2 Å. Furthermore, the DFT calculations

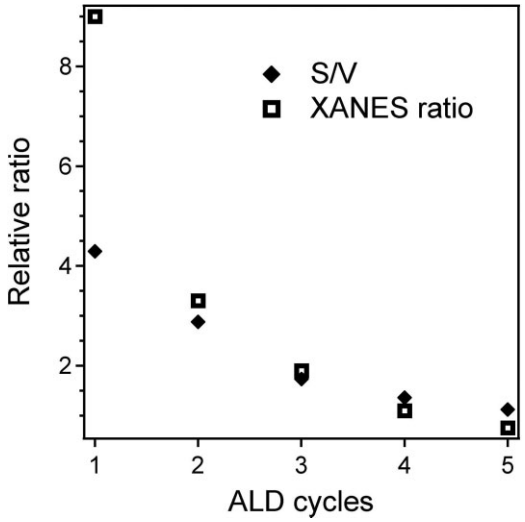

Figure 9. Comparison of the surface area to volume ratio (S/V) with the XANES ratio of Pt–O to Pt–Pt bonding. The data sets are in good agreement for two to four ALD cycles. The case of one ALD cycle is limited as the particle size for the S/V calculation was an extrapolation from Figure 6. The behavior shown here indicates that the Pt oxidation for the small particles is due to interaction with ambient oxygen and water vapor.

expected a contraction of the Pt–O bond length as the Pt loading decreased. We measured the Pt–O bond length as 1.98 ± 0.03 Å and the Pt–O bond length for crystalline platinum(II) oxide is also ≈2 Å. Since there appears to be no systematic change in the ALD Pt–O bond that may be compared to the DFT results for $SrTiO_3$ lattice oxygen, the nanoparticle oxidation may likely come through interaction with the environment. Along with the nanoparticle size, the platinum coordination decreases with the number of ALD cycles. As noted above, the size and coordination were related to an increase in the susceptibility to OH adsorption.[32] Oxidation by the environment, through interaction with ambient water vapor and/or oxygen, may result upon removal of the sample from the reactor.

The surface area to volume ratio (S/V) of the Pt nanoparticles becomes a determining factor for oxidation by the environment. If the Pt–O bond results from surface oxidation of the Pt nanoparticles following ambient exposure, then presumably the number of Pt–O versus Pt–Pt bonds should scale as S/V. Figure 9 shows a plot of S/V based on the nanoparticle size measurements from WAXS for a hemispherical particle compared against the relative ratios of Pt–O to Pt–Pt from the XANES analysis. The comparison is quite good with the exception of one ALD cycle, which may be due to the fact that this is based on an extrapolation of the particle size and the particle may in fact be smaller than 0.7 nm. Furthermore, the oxidation of the smaller nanoparticles, and consequently the effect on the chemical state, will presumably be more dramatic for the smaller nanoparticles as they have less platinum to compensate the electron affinity of the O_2 and OH. Thus, it seems likely that nanoparticles of this size are susceptible to oxidation by the ambient environment.

4. Conclusions

We have investigated the ALD of platinum nanoparticles on cube-shaped STO nanoparticles. Nanostructured materials of this nature offer some significant advantages for application in the fuel cell and catalyst fields. These advantages are tied to the nanoscale structure, morphology, and chemical state of the system. In accordance with this, we have characterized the deposition at this length scale by using SEM, SAXS, WAXS, and XAS. The Pt nanoparticles have a size of $\approx$0.7–3 nm controlled by the number of ALD growth cycles and are well dispersed on the support. The loading of the platinum is extremely efficient, $\approx 10^{-3}$ mg cm^{-2}. The nanoparticles also show a Pt–Pt bond contraction and a tendency to become oxidized as the number of ALD cycles decreases. This work demonstrates the flexibility that ALD offers to address many important issues in noble-metal nanoparticle catalysis.

5. Experimental Section

ALD Pt/STO nanocube preparation: $SrTiO_3$ nanocubes were synthesized by following a sol precipitation–hydrothermal treatment procedure described in Ref. [17], but the autoclave step was conducted for 36 h instead of 24 h. In the ALD process, the nanocubes ($\approx$0.25 g) were spread onto a stainless steel tray that was covered by a stainless steel mesh during deposition.[39] After loading into the viscous-flow ALD reactor,[40] the $SrTiO_3$ nanocubes were cleaned in situ with a flow (400 sccm) of ozone in oxygen (10% O_3) at a constant temperature (300 °C). The ALD of Pt was accomplished by using alternating exposures to $MeCpPtMe_3$ and oxygen at a constant temperature (300 °C).[27] During ALD, a constant flow (90 sccm) of ultrahigh-purity nitrogen (99.995%) carrier gas was passed through the reactor at a constant pressure (0.90 Torr). The $MeCpPtMe_3$ precursor was heated (50 °C) in a stainless steel bubbler to increase the vapor pressure. The reactant exposures lasted 200 s with partial pressures of 0.05 Torr for $MeCpPtMe_3$ and 0.20 Torr for oxygen, and nitrogen purges of 50 s were used between each exposure. For each sample, the mass was measured with an analytical balance before and after ALD to determine the Pt loading. The $SrTiO_3$ nanocubes were examined before and after the ALD of Pt by SEM using a Hitachi S4700 microscope with a field-emission gun electron-beam source.

X-ray experiments: All X-ray data sets were collected at the Advanced Photon Source (APS) of Argonne National Laboratory. The powder samples and reference materials were uniformly spread onto transparent tape (3M) and then folded to achieve appropriate signal levels for the respective scattering and absorption measurements, both taken in transmission mode. A transparent tape background was collected and removed from the X-ray scattering data.

The SAXS data sets were collected at the APS 12ID-C undulator station with a MAR 165 CCD detector (2048 $\times$ 2048 pixels), where the incident photon energy ($E_\gamma = 12.00$ keV; $\lambda = 1.033$ Å) was selected with a Si(111) monochromator. A series of slits collimated the beam to a size of approximately 100 mm (horizontal) by 50 mm (vertical). The momentum transfer was calibrated by using a silver behenate standard and the detector-to-sample distance was 2.13 m.

The WAXS data were collected at the APS 5ID-D undulator beamline with a dual-chip 100 $\times$ 200 mm^2 Roper CCD detector. The incident photon energy ($E_\gamma = 16.005$ keV; $\lambda = 0.77466$ Å) was selected by using a Si(111) monochromator and the beam was further collimated with three slits to give a size of approximately 0.2 $\times$ 0.2 mm^2. The detector position relative to the source was calibrated with a silicon diffraction grating (3600 lines mm^{-2}; LightSmyth Technologies, no. SLG-C36-1212-Si). This allowed the determination of the momentum transfer calibration and sample-to-detector distance (235 mm).

The XAS measurements were carried out around the Pt L_3 edge ($E_0 = 11.564$ keV) at the bending magnet beamline of the DND-CAT (5BM-D). The X-ray absorption spectra were collected in fluorescence mode by using a xenon-filled Lytle cell and a Zn filter to minimize the scattering signals. The X-ray absorption spectra of the reference materials were collected in transmission mode by using gas ionization chambers (Oxford Danfysik). The X-ray photon energy was calibrated with a Pt metal foil. During the XAS measurements, the energy stability was regularly monitored by simultaneously measuring the Pt foil, which was placed in between the second and third ion chambers. The X-ray absorption spectra were all measured from -200 eV below to 1000 eV ($k \approx 16$ Å^{-1}) above the absorption edge. The near-edge spectra were collected with an energy step of 0.5 eV. Data processing was performed with the ATHENA program.[29]

Acknowledgements

This work was supported by the Institute for Catalysis in Energy Processes, Northwestern University (NU) (US Department of Energy Grant DE-FG02-03ER15457) and by facilities support from the NU Materials Research Center (National Science Foundation MRSEC Grant DMR-0520513). Argonne National Laboratory (ANL) is a US Department of Energy Office of Science Laboratory operated under Contract No. DE-AC02-06CH11357 by UChicago Argonne, LLC. X-ray measurements were performed at ANL's Advanced Photon Source, Sector 12 (BESSRC), and at Sector 5 (DND-CAT) which is supported in part by: E. I. DuPont de Nemours & Co., Dow Chemical Co., and the State of Illinois. Electron microscopy was performed at ANL's Electron Microscopy Center for Materials Research.

[1] H. S. Liu, C. J. Song, L. Zhang, J. J. Zhang, H. J. Wang, D. P. Wilkinson, *J. Power Sources* **2006**, *155*, 95–110.
[2] X. R. Jiang, H. Huang, F. B. Prinz, S. F. Bent, *Chem. Mater.* **2008**, *20*, 3897–3905.
[3] S. Alayoglu, A. U. Nilekar, M. Mavrikakis, B. Eichhorn, *Nat. Mater.* **2008**, *7*, 333–338.
[4] M. A. Fox, M. T. Dulay, *Chem. Rev.* **1993**, *93*, 341–357.
[5] L. Yuliati, H. Yoshida, *Chem. Soc. Rev.* **2008**, *37*, 1592–1602.
[6] H. Yoshida, Y. Yazawa, T. Hattori, *Catal. Today* **2003**, *87*, 19–28.
[7] M. Lashdaf, J. Lahtinen, M. Lindblad, M. Tiitta, T. Venalainen, H. Osterholm, *Stud. Surf. Sci. Catal.* **2004**, *154*, 1708–1713.

[8] A. T. Bell, *Science* **2003**, *299*, 1688–1691.
[9] M. S. Dresselhaus, I. L. Thomas, *Nature* **2001**, *414*, 332–337.
[10] M. Ritala, M. Leskela, in *Handbook of Thin Film Materials*, Vol. 1 (Ed.: H. S. Nalwa), Academic Press, San Diego **2002**, p. 103.
[11] S. Haukka, E.-L. Lakomaa, T. Suntola, in *Adsorption and its Applications in Industry and Environmental Protection* (Ed.: A. Dabrowski), *Stud. Surf. Sci. Catal*, Vol. 120A, Elsevier, Amsterdam **1999**.
[12] J. W. Elam, A. Zinovev, C. Y. Han, H. H. Wang, U. Welp, J. N. Hryn, M. J. Pellin, *Thin Solid Films* **2006**, *515*, 1664–1673.
[13] A. Johansson, J. Lu, J. O. Carlsson, M. Boman, *J. Appl. Phys.* **2004**, *96*, 5189–5194.
[14] J. S. King, A. Wittstock, J. Biener, S. O. Kucheyev, Y. M. Wang, T. F. Baumann, S. K. Giri, A. V. Hamza, M. Baeumer, S. F. Bent, *Nano Lett.* **2008**, *8*, 2405–2409.
[15] Y. Zhu, K. A. Dunn, A. E. Kaloyeros, *J. Mater. Res.* **2007**, *22*, 1292–1298.
[16] J. Greeley, M. Mavrikakis, *Nat. Mater.* **2004**, *3*, 810–815.
[17] F. A. Rabuffetti, H.-S. Kim, J. A. Enterkin, Y. Wang, C. H. Lanier, L. D. Marks, K. R. Poeppelmeier, P. C. Stair, *Chem. Mater.* **2008**, *20*, 5628–5635.
[18] B. Aurian-Blajeni, M. Halmann, J. Manassen, *Solar Energy* **1980**, *25*, 165–170.
[19] R. G. Carr, G. A. Somorjai, *Nature* **1981**, *290*, 576–577.
[20] A. H. A. Tinnemans, T. P. M. Koster, D. H. M. W. Thewissen, A. Mackor, *Nouv. J. Chim.* **1982**, *6*, 373–379.
[21] W. Setthpun, F. A. Rabuffetti, J. W. Elam, P. C. Stair, K. R. Poeppelmeier, C. L. Marshall, unpublished.
[22] A. L. Linsebigler, G. Q. Lu, J. T. Yates, *Chem. Rev.* **1995**, *95*, 735–758.
[23] K. Takehira, T. Shishido, M. Kondo, *J. Catal.* **2002**, *207*, 307–316.
[24] Y. B. Mao, S. Banerjee, S. S. Wong, *J. Am. Chem. Soc.* **2003**, *125*, 15718–15719.
[25] S. T. Christensen, J. W. Elam, B. Lee, Z. Feng, M. J. Bedzyk, M. C. Hersam, *Chem. Mater*, **2009**, *21*, 516–521.
[26] T. Aaltonen, A. Rahtu, M. Ritala, M. Leskela, *Electrochem. Solid-State Lett.* **2003**, *6*, C130–C133.
[27] T. Aaltonen, M. Ritala, T. Sajavaara, J. Keinonen, M. Leskela, *Chem. Mater.* **2003**, *15*, 1924–1928.
[28] B. E. Warren, *X-ray Diffraction*, Dover, New York 1990.
[29] B. Ravel, M. Newville, *J. Synchrotron Radiat.* **2005**, *12*, 537–541.
[30] W. J. Moore, L. Pauling, *J. Am. Chem. Soc.* **1941**, *63*, 1392–1394.
[31] T. Frelink, W. Visscher, J. A. R. Vanveen, *J. Electroanal. Chem.* **1995**, *382*, 65–72.
[32] S. Mukerjee, J. McBreen, *J. Electroanal. Chem.* **1998**, *448*, 163–171.
[33] S. Park, Y. Xie, M. J. Weaver, *Langmuir* **2002**, *18*, 5792–5798.
[34] M. Klimenkov, S. Nepijko, H. Kuhlenbeck, M. Baumer, R. Schlogl, H. J. Freund, *Surf. Sci.* **1997**, *391*, 27–36.
[35] M. K. Oudenhuijzen, J. H. Bitter, D. C. Koningsberger, *J. Phys. Chem. B* **2001**, *105*, 4616–4622.
[36] J. T. Miller, A. J. Kropf, Y. Zha, J. R. Regalbuto, L. Delannoy, C. Louis, E. Bus, J. A. van Bokhoven, *J. Catal.* **2006**, *240*, 222–234.
[37] T. Aaltonen, M. Ritala, Y. L. Tung, Y. Chi, K. Arstila, K. Meinander, M. Leskela, *J. Mater. Res.* **2004**, *19*, 3353–3358.
[38] A. Asthagiri, D. S. Sholl, *J. Chem. Phys.* **2002**, *116*, 9914–9925.
[39] J. A. Libera, J. W. Elam, M. J. Pellin, *Thin Solid Films* **2008**, *516*, 6158–6166.
[40] J. W. Elam, M. D. Groner, S. M. George, *Rev. Sci. Instrum.* **2002**, *73*, 2981–2987.

Received: December 19, 2008

